Spg20−/− mice reveal multimodal functions for Troyer syndrome protein spartin in lipid droplet maintenance, cytokinesis and BMP signaling

Benoît Renvoisé[1], Julia Stadler[1], Rajat Singh[1], Joanna C. Bakowska[2],* and Craig Blackstone[1],*

[1]Cell Biology Section, Neurogenetics Branch, National Institute of Neurological Disorders and Stroke, National Institutes of Health, Bethesda, MD 20892 and [2]Department of Pharmacology and Experimental Therapeutics, Loyola University Chicago Stritch School of Medicine, Maywood, IL 60153, USA

Hereditary spastic paraplegias (HSPs; SPG1-48) are inherited neurological disorders characterized by lower extremity spasticity and weakness. Loss-of-function mutations in the *SPG20* gene encoding spartin cause autosomal recessive Troyer syndrome (SPG20), which has additional features of short stature, cognitive deficits and distal amyotrophy. To identify cellular impairments underlying Troyer syndrome, we generated *Spg20−/−* mice, which exhibit progressive gait defects. Although gross central nervous system pathology appeared largely normal, cerebral cortical neurons cultured from neonatal *Spg20−/−* mice exhibited increased axon branching, a phenotype suppressed by reintroducing spartin and which required its interaction with the <u>e</u>ndosomal <u>s</u>orting <u>c</u>omplex <u>r</u>equired for <u>t</u>ransport (ESCRT)-III protein IST1. Analysis of the bone morphogenetic protein (BMP) signaling pathway in *Spg20−/−* embryonic fibroblasts indicated that Smad1/5 phosphorylation is modestly elevated, possibly due to alterations in BMP receptor trafficking. Cytokinesis was impaired in embryonic fibroblasts cultured from *Spg20−/−* mice, and binucleated chondrocytes were prominent in epiphyseal growth plates of bones in *Spg20−/−* mice, perhaps explaining the short stature of patients. Finally, adipose tissue from *Spg20−/−* female mice exhibited increased lipid droplet (LD) numbers and alterations in perilipin levels, supporting a role for spartin in LD maintenance. Taken together, our results support multimodal functions for spartin that provide important insights into HSP pathogenesis.

INTRODUCTION

Hereditary spastic paraplegias (HSPs) are a genetically diverse group of neurological disorders with the cardinal feature of lower extremity spastic weakness, resulting from a distal axonopathy of corticospinal motor neurons (1,2). HSPs have historically been divided into two categories, 'pure' or 'complicated', based on the presence (complicated) or absence (pure) of associated clinical features such as cognitive dysfunction, distal amyotrophy, thin corpus callosum, white matter abnormalities and neuropathy (3). More recently, a genetic classification scheme has taken hold, with well over 40 distinct loci mapped (*SPG1-48*) (2). Greater than 20 HSP genes and their protein products have now been identified, and sequence

analyses and published studies support pathogenic convergence within a number of common cellular themes, including alterations in endoplasmic reticulum (ER) network shaping/ distribution, lipid/cholestrol metabolism, mitochondrial function, myelination, bone morphogenetic protein (BMP) signaling, adaptor protein function and endocytosis (1,2,4–9).

Troyer syndrome (SPG20; OMIM 275900) is a childhood-onset, autosomal recessive, complicated HSP characterized by spastic paraparesis along with spastic dysarthria, cognitive impairment, short stature and distal amyotrophy, exhibiting both developmental and degenerative features (10–14). Nearly all patients have been described within Old Order Amish communities in Ohio (12), but more recently a different mutation was identified in an Omani kindred (14). In all known

*To whom correspondence should be addressed at: Neurogenetics Branch, NINDS, NIH Building 35, Room 2C-913, 9000 Rockville Pike, Bethesda, MD 20892-3738, USA. Tel: +1 3014519680; Fax: +1 3014804888; E-mail: blackstc@ninds.nih.gov (C.B.); Department of Pharmacology, Loyola University Chicago Stritch School of Medicine, 2160 S. First Ave., Bldg. 102, Room 3636, Maywood, IL 60153, USA. Tel: +1 7082168427; E-mail: jbakowska@lumc.edu (J.B.)

cases, the disorder is caused by frameshift mutation of *SPG20* resulting in large predicted protein truncations and complete loss of expression of spartin, the *SPG20* gene product (11–14).

Spartin is a 666-amino-acid residue protein widely expressed in human tissues and broadly conserved among species (Fig. 1A); it localizes to several different cellular organelles and compartments, including endosomes, midbodies, lipid droplets (LDs), and mitochondria (15–22). Spartin harbors an N-terminal MIT (contained within microtubule-interacting and trafficking molecules) domain (23), a proline-rich PY motif and a plant-related senescence domain (Fig. 1B). Its MIT domain interacts selectively with the endosomal ESCRT-III protein IST1 (21), while the PY domain interacts with the WW domains of Nedd4-family ubiquitin ligases such as atrophin-1-interacting protein 4 (AIP4) and AIP5 (18,19,24). The ESCRT-III complex is the core machinery mediating membrane abscission events in ESCRT-dependent pathways, including multivesicular body formation, viral budding and membrane abscission during cytokinesis (25), while Nedd4-family E3 ligases function in ubiquitin-dependent, proteasome-mediated protein degradation (26).

Concordant with its distributions among different organelles, spartin has been implicated in multiple cellular processes. Spartin participates in cytokinesis and is recruited to midbodies via its interaction with IST1 (21). Spartin is also monoubiquitinated, recruited to endosomes and required for efficient endosomal trafficking and degradation of the epidermal growth factor receptor (EGFR) in HeLa cells (17,19). Finally, spartin localizes to newly formed LDs (18,19,24), dynamic lipid-storage organelles formed via the accumulation of neutral lipids at the ER and recruitment of specific proteins, including perilipin family-members. Spartin interacts with the surface lipid monolayer of LDs through its C-terminal region and plays a role in LD regulation by binding to TIP47 and E3 ubiquitin ligases (such as AIP4 and AIP5) on LDs (17–19,24,27), with these interaction leading to degradation of LD-associated proteins (24,27).

Recently, spartin was shown to inhibit the BMP signaling pathway, a function shared among other HSP proteins, including atlastin-1 (SPG3A), spastin (SPG4) and NIPA1 (SPG6) (28). These alterations are particularly interesting with respect to disease pathogenesis as BMP signaling is a crucial pathway for neuronal development and axonal function. Studies in *Drosophila* have shown a determinant role for BMP signaling in synaptic growth at the neuromuscular junction, and BMP signaling regulates axonal growth, guidance and differentiation during mammalian development (29–32).

In this study, we have developed a mouse model for Troyer syndrome by targeted disruption of the *Spg20* gene. *Spg20*−/− mice have a significant gait phenotype behaviorally, and this is associated with a number of disease-relevant cellular abnormalities affecting axon branching in cerebral cortical neurons, LD maintenance, cytokinesis and BMP signaling.

RESULTS

Adult *Spg20*−/− mice exhibit motor dysfunction

Spartin is a highly conserved protein, with putative orthologs present in distant species (Fig. 1A); its domain organization is shown schematically in Figure 1B. As Troyer syndrome patients lack spartin protein (13,14), we generated *Spg20* null mice to analyze the pathophysiology of Troyer syndrome. *Spg20*−/− mice were generated by homologous recombination using the strategy shown in Figure 1C. Disruption of *Spg20* was confirmed using polymerase chain reaction (PCR) (data not shown), and immunoblotting of brain, spinal cord and testis tissue homogenates from *Spg20*−/− adult mice revealed an absence of spartin protein (Fig. 1D).

Spg20−/− mice breed normally, and their offspring appear normal in the cage at birth. However, they develop progressive impairments in motor function. To assess lower extremity tone, we compared *Spg20*−/− and *Spg20*+/+ mice at multiple ages (2–12 months) using a suspension reflex test. The hind limb phenotype upon suspending animals by the tail was significantly different in 12-month-old *Spg20*−/− mice when compared with age-matched *Spg20*+/+ mice (Fig. 1E and F and Supplementary Material, Videos S1 [Spg20+/+] and S2 [Spg20−/−]). Furthermore, at 4–7 months of age both male and female *Spg20*−/− mice showed decreases in duration and maximum speed on Rotarod testing (Fig. 1G and H and Supplementary Material, Videos S3 [male] and S4 [female], with *Spg20*+/+ mice on the left and *Spg20*−/− mice on the right in each video clip). Hind limb strength was less affected, and differences were significant only in female mice within this age range (Fig. 1I).

Central nervous system pathology in *Spg20*−/− mice

Six *Spg20*−/− (three male, three female) mice and an equal number of aged- and sex-matched *Spg20*+/+ mice were pathologically phenotyped by the NIH Office of Research Services Veterinary Research Program, with a comprehensive analysis comprising organ weights, serum chemistries, gross pathology and histological stains. The final report summaries are appended as Supplementary Material, Figure S1 and S2. Serum studies detailed in Supplementary Material, Table S1 showed statistically significant reductions in triglyceride ($P = 0.018$) and uric acid ($P = 0.015$) levels in male *Spg20*−/− mice compared with *Spg20*+/+ mice, though these values were all within the normal range.

To assess the consequences of the absence of spartin in the central nervous system of *Spg20*−/− mice, we perfused 12-month-old *Spg20*+/+ and *Spg20*−/− mice ($n = 3$ of each) with paraformaldehyde and extracted brains and spinal cords. Whole brain measurements (Fig. 2A) did not shown significant differences in brain size. Nissl- and H&E-stained parasagittal sections (Fig. 2B and C) revealed no visible differences between deep nuclei and cortical layers of *Spg20*+/+ and *Spg20*−/− mice. Staining with cresyl violet (for cell soma) and luxol fast blue (for myelin) also showed no significant differences among brain and spinal cord sections of *Spg20*+/+ and *Spg20*−/− mice, and spinal cord anterior horn cell number was unchanged (Fig. 2C and D and data not shown). Analysis of the axon termini of lower motor neurons (Supplementary Material, Fig. S3) showed that the neuromuscular junction, end plates and synaptic size appeared similar. We identified one *Spg20*−/− mouse with prominent paresis of the right front leg and bilateral hind limbs at 6 months of age due to a mesenchymal cell neoplasm composed
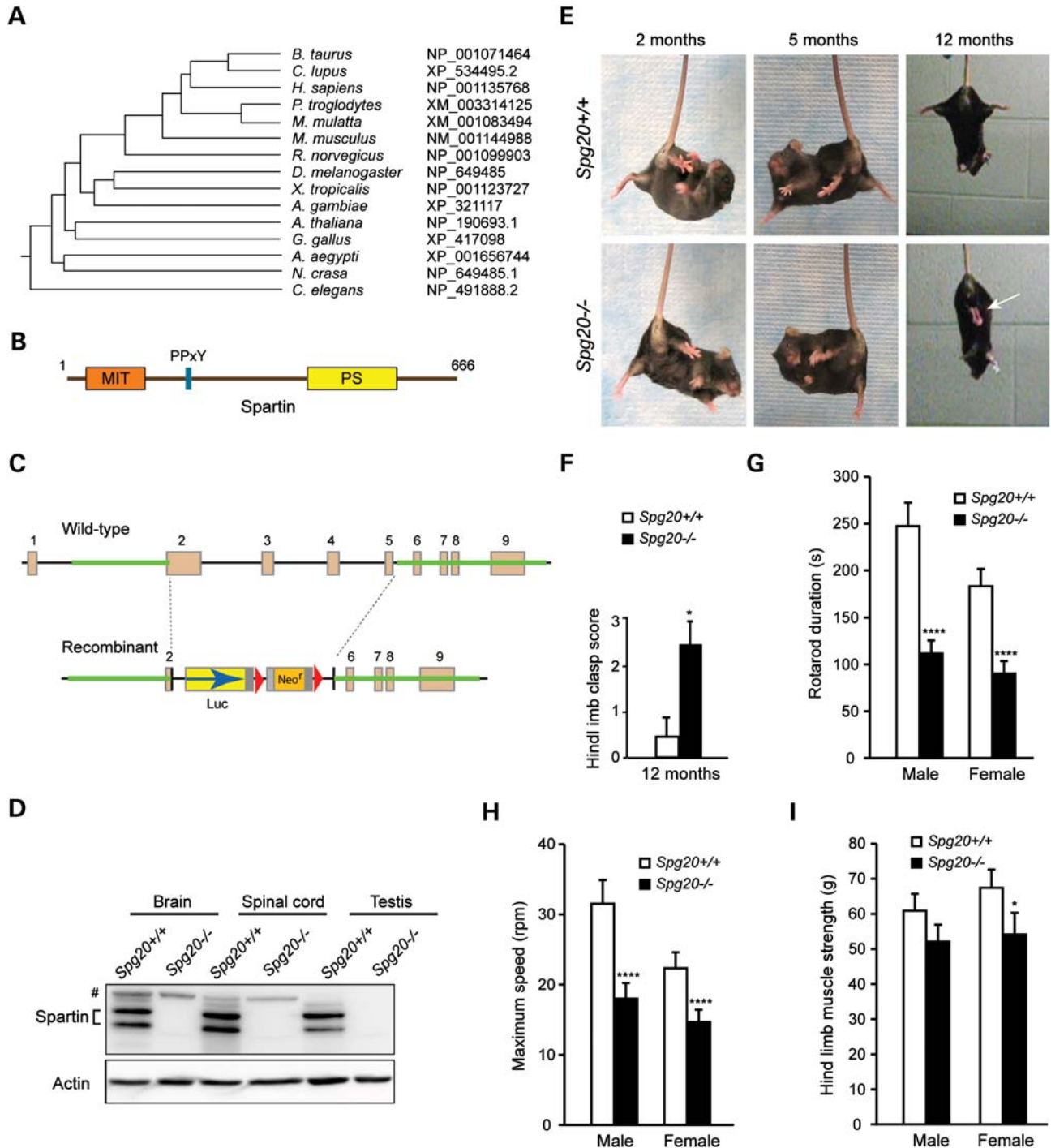
Figure 1. Generation of *Spg20−/−* knock out mice. (**A**) Spartin phylogenetic tree. Species and GenBank protein accession numbers are shown. The tree was constructed using ClustalW (v1.4). (**B**) Schematic diagram of spartin. MIT, present in microtubule-interacting and trafficking proteins; PS, plant-related senescence domain. Amino acid residue numbers are shown along the top. (**C**) Generation of *Spg20−/−* mice. Schematic representation of the *Spg20* gene targeting strategy, with *Spg20* exons numbered. Luc, luciferase; Neo^r, neomycin resistance. (**D**) Immunoblot analysis of spartin protein in brain, spinal cord and testis lysates from adult *Spg20+/+* and *Spg20−/−* mice. Actin levels were monitored as a control for protein loading. # denotes a cross-reactive protein band. (**E**) Suspension reflex testing of *Spg20+/+* and *Spg20−/−* mice at 2, 5 and 12 months of age. An arrow denotes clasped hind limbs. (**F**) Quantification of hind limb clasping at 12 months (means ± SD). Scores were tallied after suspending mice by the tail: 0, normal; 1, hind limbs touching for 1–15 s; 2, hindlimbs touching for 16–30 s; 3, hindlimbs touching for >30 s. (**G and H**) Rotarod testing of *Spg20+/+* ($n = 24$) and *Spg20−/−* ($n = 44$) mice at 4–7 months of age, with quantification of duration (G) and maximum speed (H), means ± SD. (**I**) Hind limb muscle strength was quantitated in *Spg20+/+* and *Spg20−/−* mice at 4–7 months of age ($n = 24$ and 44, respectively). $^*P < 0.05$; $^{****}P < 0.001$.
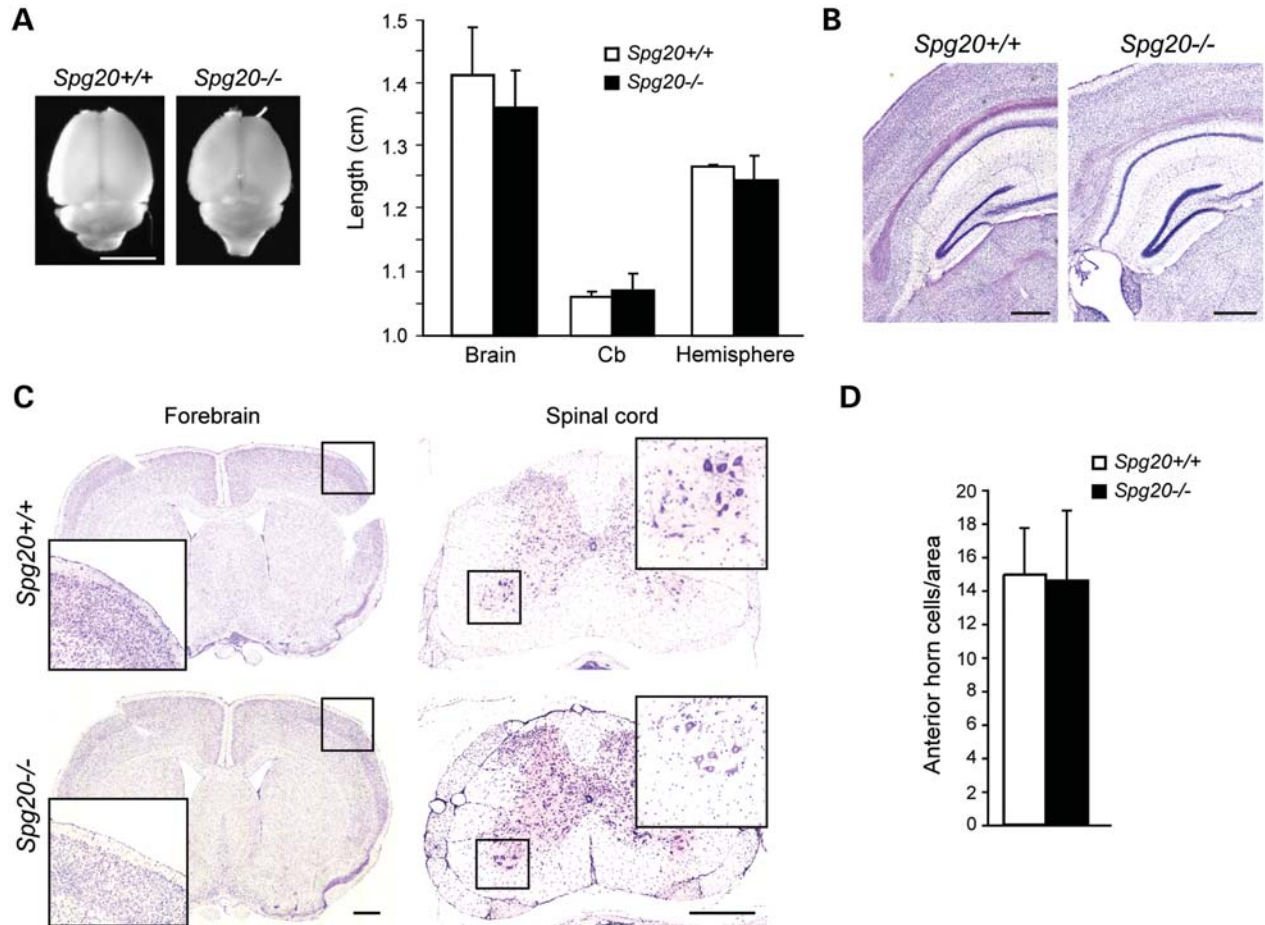
Figure 2. Neuropathologic analysis of *Spg20−/−* mice. (**A**) Dorsal view of whole-mount adult brain (left) and measurements of whole-mount brain, cerebellum (Cb) and cerebral hemisphere length (right). Left and right sides of brain were measured as replicates, and average lengths were calculated. Means ± SD are graphed (*n* = 3 animals per genotype). Scale bar, 1 cm. (**B**) Nissl-stained parasagittal sections of brains from *Spg20+/+* and *Spg20−/−* adult mice. Scale bar, 50 μm. (**C**) Left, parasagittal sections of mouse brains stained with H&E. Right, parasagittal sections of cervical spinal cord were stained with cresyl violet. Boxed regions are enlarged in the insets. Scale bar, 500 μm. (**D**) Relative number of spinal cord anterior horn cells was quantified per 0.6 cm^2 area (means ± SD; *n* = 3).

of spindle to oval cells compressing the cervical spinal cord and tracking along nerve roots as well as along the base of the brain and into the fourth ventricle (Supplementary Material, Fig. S4).

Cultured cortical neurons from *Spg20−/−* mice exhibit increased branching

As a number of mammalian cell culture models for HSPs have exhibited alterations in neuronal morphology, particularly axon elongation and branching (32–35), we assessed *Spg20−/−* neuronal morphology (Fig. 3 and Supplementary Material, Fig. S5). In *Spg20+/+* cerebral cortical neurons in primary culture, spartin was observed in the cell soma and axon, while *Spg20−/−* neurons did not have detectable spartin protein by immunostaining or immunoblotting (Fig. 3A and B). Immunostaining of neurons for Tau-1 (axonal marker) and MAP2 (dendritic marker) facilitated assessment of cellular morphology (Supplementary Material, Fig. S5A and B). Quantification of cell form (degree of roundness), bipolarity (degree of cellular elongation) and spreading

index as described in Materials and Methods showed close similarities between cortical neurons cultured from *Spg20+/+* and *Spg20−/−* mice (Supplementary Material, Fig. S5C). However, axon length and branching (primary and secondary) were significantly greater in *Spg20−/−* neurons (Fig. 3C and D), and the number of dendrites per neuron also showed significant increases in *Spg20−/−* versus *Spg20+/+* neurons (Fig. 3E). Taken together, our results are highly reminiscent of those described in neurons cultured from mice modeling the complicated hereditary spastic paraplegia (HSP) Mast syndrome (*Spg21−/−*; ref. 36), and they indicate that spartin may similarly function as a negative regulator of axon and dendrite formation and branching.

Suppression of *Spg20−/−* branching phenotype by spartin requires interaction with ESCRT-III

The ESCRT machinery (ESCRT-0 through ESCRT-III) is involved in a number of membrane modeling events, including multivesicular body formation, viral budding and abscission during cytokinesis (25). Of the 12 known human ESCRT-III
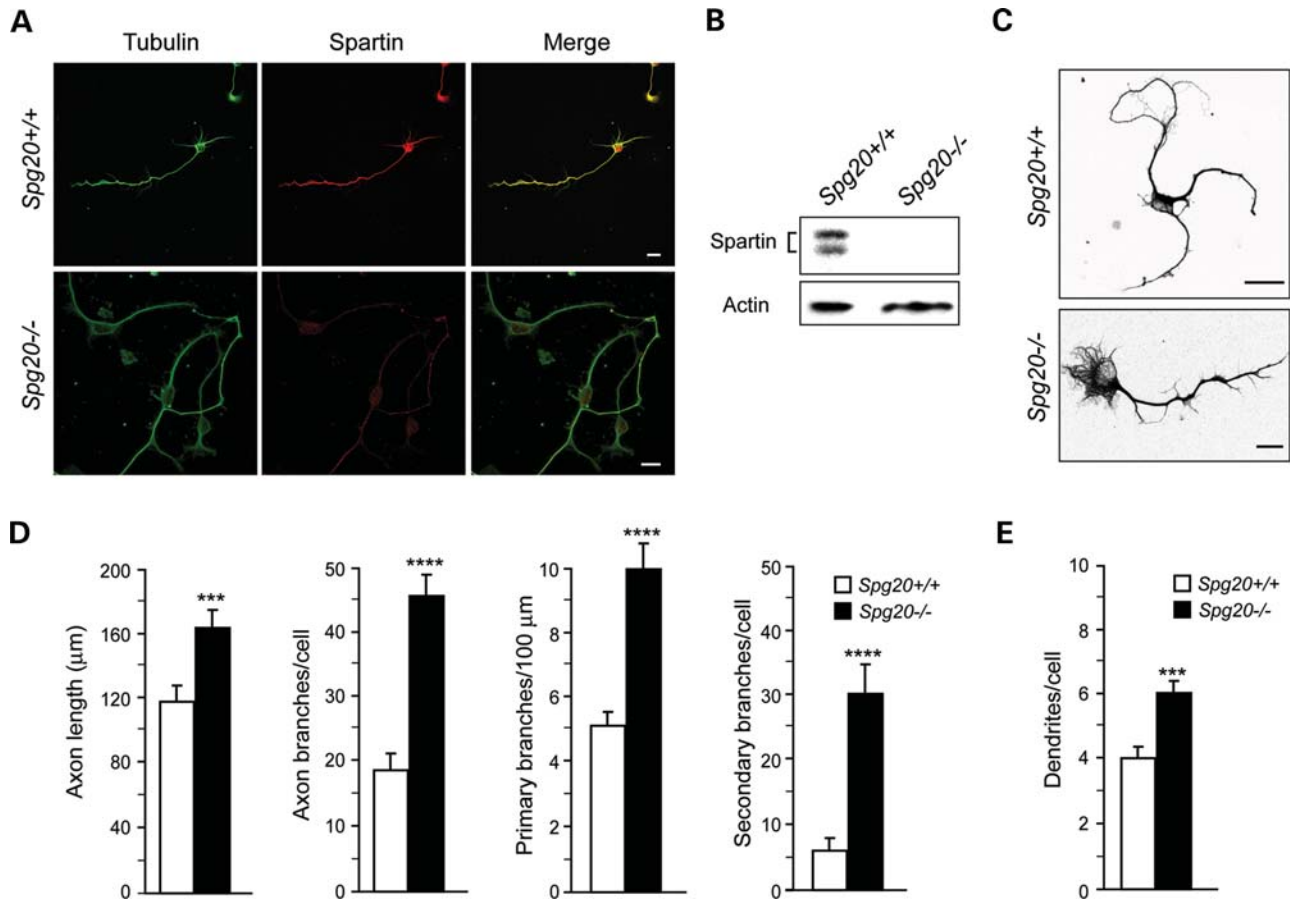
Figure 3. Cerebral cortical neurons cultured from *Spg20−/−* mice exhibit increased axon branching. (**A**) Representative neurons at DIV3 were co-stained for β-tubulin (green) and endogenous spartin (red). The merged image is at the right. Scale bar, 10 μm. (**B**) Immunoblot analysis of spartin protein in total lysates from *Spg20+/+* and *Spg20−/−* cortical neurons. Actin levels were monitored as a control for protein loading. (**C**) β-tubulin staining (black) reveals processes of *Spg20+/+* and *Spg20−/−* cultured neurons at DIV3. Scale bar, 20 μm. (**D**) Quantifications of primary axon length as well as number of total, primary, and secondary axon branches in *Spg20+/+* and *Spg20−/−* DIV3 cortical neurons in primary culture (means ± SD; $n = 3$, with 30–60 neurons per trial). (**E**) Numbers of dendrites per cell are shown graphically (means ± SD; $n = 3$, with 30–60 neurons per trial). ***$P < 0.005$, ****$P < 0.001$.

subunits, only IST1 interacts with the MIT domain of spartin (21). To study the role of spartin in axon branching, we analyzed its interaction with IST1, which is required for spartin recruitment to midbodies during cytokinesis (21). Immunoblotting of total homogenates from *Spg20+/+* and *Spg20−/−* brain and spinal cord showed that IST1 protein levels are similar (Fig. 4A). Moreover, cellular distributions of IST1 in cerebral cortical neurons cultured from *Spg20+/+* and *Spg20−/−* mice appeared the same (Fig. 4B). Thus, the expression and distributions of IST1 seem independent of spartin. The spartin MIT domain interaction with IST1 requires Phe24 (F24), and a structure-based F24D mutation (Fig. 4C) abolishes the interaction of spartin with IST1 (21,37). Expression of hemagglutinin (HA)-tagged spartin rescues the increased branching phenotype in *Spg20−/−* neurons, reducing axon branch numbers to levels observed in *Spg20+/+* neurons (Fig. 4D and E). In contrast, expression of HA-tagged mutant spartin F24D did not affect the number of branches in *Spg20−/−* neurons. Lastly, overexpression of HA-IST1 significantly increased the number of axon branches in *Spg20−/−* neurons when compared with those neurons transfected with a control vector (Fig. 4D and E). Together, these data suggest that

spartin may negatively regulate the activity of IST1 in stimulating axonal branching.

Lack of spartin increases accumulation of LDs

Spartin has been implicated in the regulation of LDs (18,19,24). To investigate the role of spartin on LD maintenance *in vivo*, we analyzed weights of *Spg20+/+* and *Spg20−/−* mice from 3 to 22 days post-delivery, but noted no significant differences (Fig. 5A). When categorized by sex, body weights of male and female mice remained similar in *Spg20+/+* and *Spg20−/−* mice at 1 month of age (Fig. 5B). However, the proportion of adipose tissue was significantly increased in *Spg20−/−* versus *Spg20+/+* female mice, while males showed no significant differences (Fig. 5B). These data suggest that spartin is particularly important for lipid metabolism in female mice. Evalaution of adipocytes in H&E-stained white adipose tissue sections showed alterations in the overall appearance of the tissue, with adipocyte sizes highly variable in the *Spg20−/−* mice. This disorganization might reflect altered proliferation and/or differentiation of the adipocytes. In fact, there was a
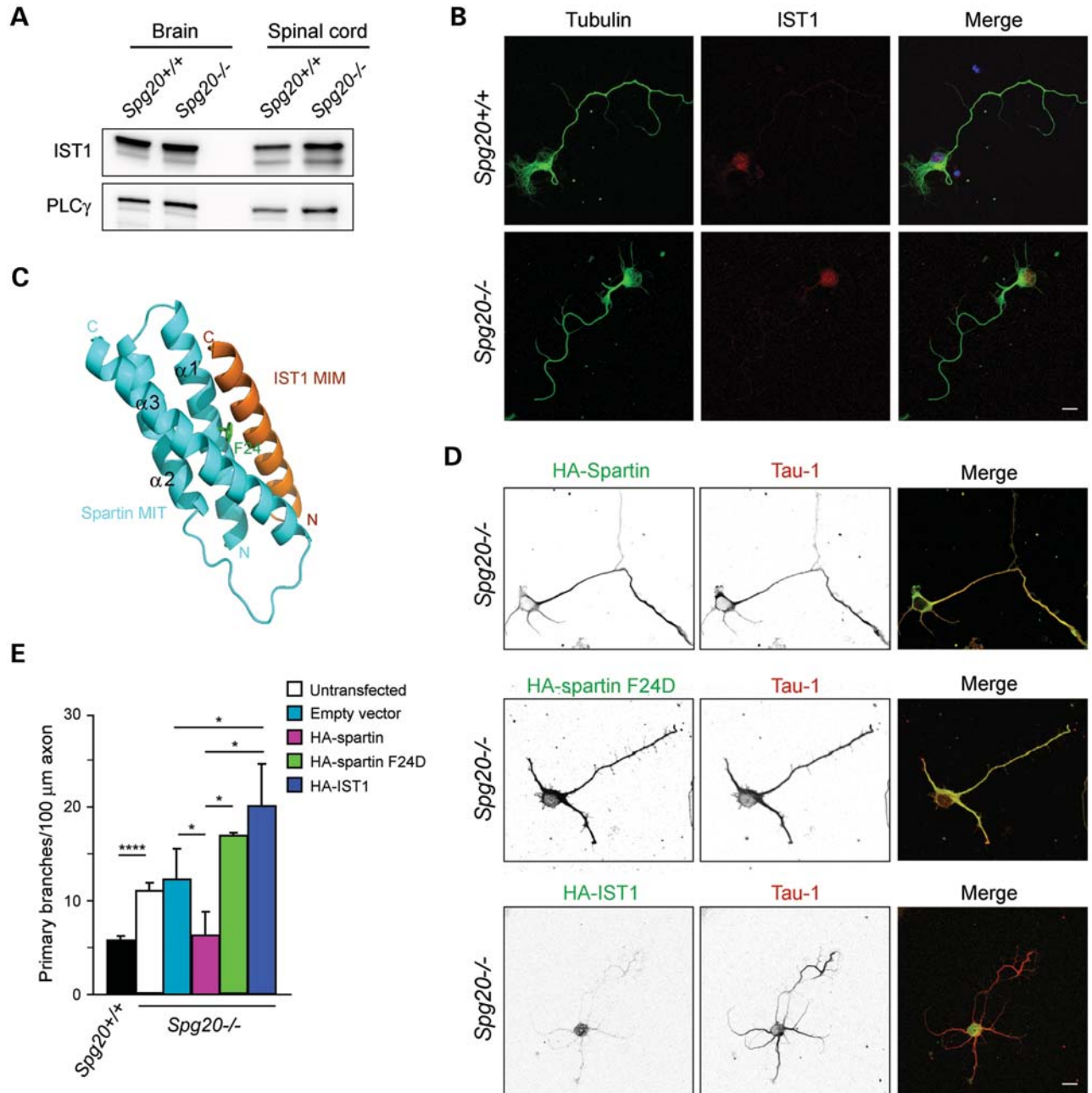
Figure 4. Interaction with the ESCRT-III protein IST1 is required for spartin-mediated effects on axonal branching. (**A**) Immunoblot of IST1 protein in total lysates from brain and spinal cord of *Spg20+/+* and *Spg20−/−* mice. PLCγ is a control for protein loading. (**B**) Representative cultured cerebral cortical neurons from *Spg20+/+* and *Spg20−/−* mice stained with β-tubulin (green) and IST1 (red). Scale bar, 20 μm. (**C**) Structural model of spartin MIT domain (blue) interacting with IST1 MIT-interacting motif (MIM; orange). Residue Phe24 (F24) in the spartin MIT domain is shown in green. Adapted from ref. 21. (**D**) *Spg20−/−* neurons overexpressing wild-type HA-spartin, HA-spartin F24D or HA-IST1 were co-stained with HA-tag (green) and Tau-1 (red) antibodies. Black and white images are at the left, and merged color images are to the right. Scale bar, 20 μm. (**E**) Quantification of number of branches per 100 μm of axon in DIV3 cortical neurons, transfected as indicated ($n = 3$, with 30 neurons per trial). The genotype is shown below. $*P < 0.005$, $****P < 0.001$.

significant increase in adipocyte number in 1-month-old *Spg20−/−* female mice, with a concomitant decrease in adipocyte size (Fig. 5C and D and data not shown). Similar changes were present in 4-month-old *Spg20−/−* females (Supplementary Material, Fig. S6A). Male *Spg20−/−* mice did not show significant differences in adipocyte number or size at either age (Supplementary Material, Fig. S6B and data not shown). While adipose tissue sections revealed that the tissue organization was disrupted at both 1 and 4 months of age in female *Spg20−/−* mice (Fig. 5C and Supplementary Material, Fig. S6C), no morphological changes were noted in the *Spg20−/−* male adipose tissue at these ages
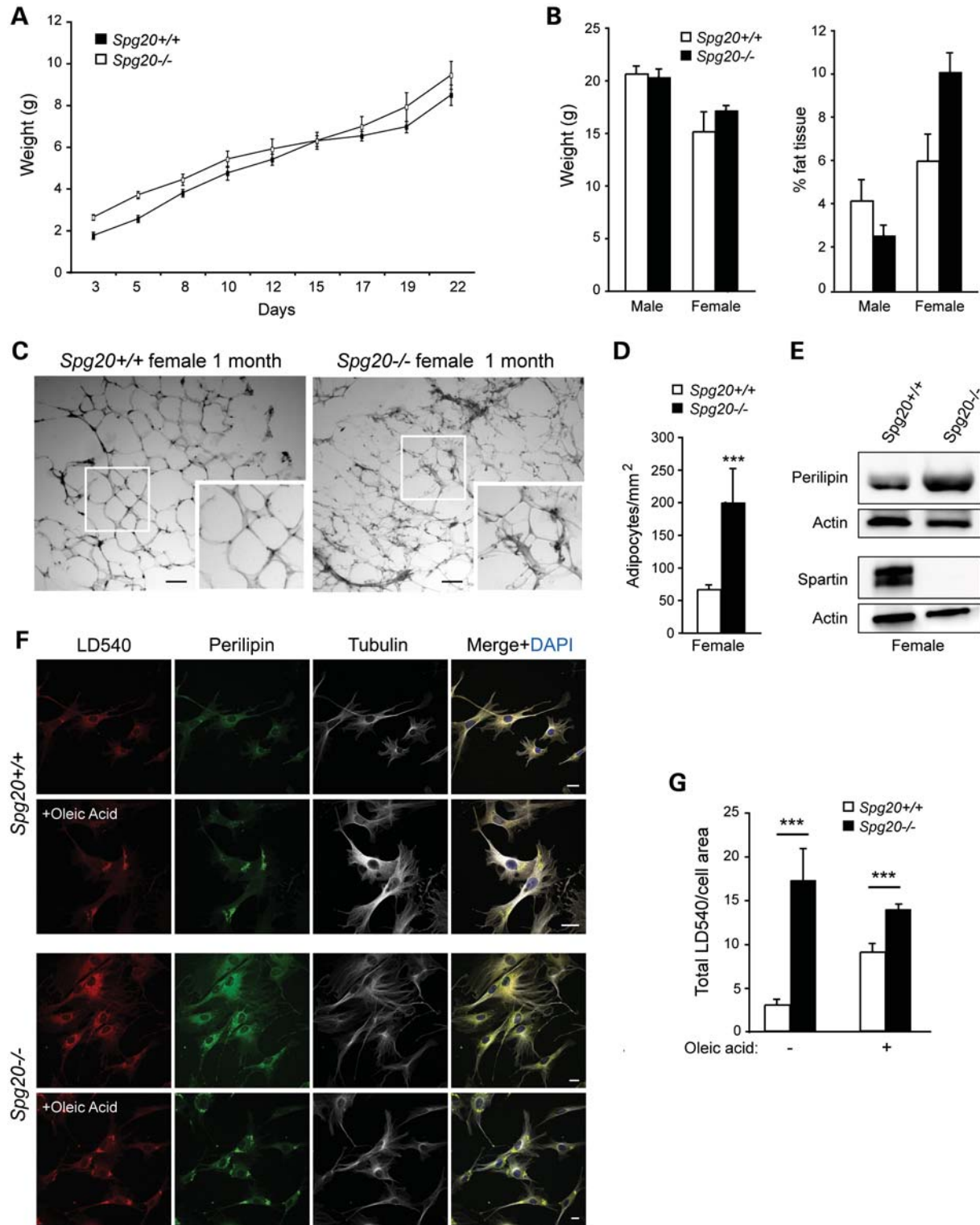
Figure 5. LD defects in *Spg20−/−* mice. (**A**) Body weight measurements of *Spg20+/+* (*n* = 9) and *Spg20−/−* (*n* = 8) mice, ages 3−22 days. (**B**) Graphical representation of weight and percentage of adipose tissue in male and female *Spg20+/+* and *Spg20−/−* mice at one month of age (means ± SD; *n* = 3). (**C**) Sections of adipose tissue in one month-old *Spg20+/+* and *Spg20−/−* female mice. Insets show enlargements of the boxed areas. Scale bar, 100 μm. (**D**) Number of adipocytes/mm² in female *Spg20+/+* and *Spg20−/−* mice. (**E**) Immunoblots of total adipose tissue lysates from 4-month-old *Spg20+/+* and *Spg20−/−* females. Actin levels were monitored as a control for protein loading. (**F**) Immunofluorescence staining of LD540, perilipin and β-tubulin on MEFs from *Spg20+/+* and *Spg20−/−* mice. Cells were treated with oleic acid where indicated. Scale bars, 10 μm. (**G**) Graphical representation of total LD540 staining intensity in *Spg20+/+* and *Spg20−/−* MEFs treated or not with oleic acid (means ± SD; *n* = 20). ***$P < 0.005$.

(Supplementary Material, Fig. S6D and data not shown). Although the reasons for these sex differences remain unclear, they may reflect hormonal differences, conceivably related to spartin-dependent alterations in estrogen signaling. Immunoblots of adipose tissue from 4-month-old *Spg20−/−* females showed an increase in levels of perilipin A, which coats LDs and is involved in regulating lipid stores, consistent with the observed increase in LD number (Fig. 5E).

To establish further the involvement of spartin in lipid metabolism, we analyzed the formation of LDs in embryonic fibroblasts from *Spg20−/−* and *Spg20+/+* mice [mouse embryonic fibroblasts (MEFs); Fig. 5F]. The fluorescence intensity of the selective LD dye LD540 was significantly higher in *Spg20−/−* cells compared with *Spg20+/+* cells (Fig. 5F and G). The application of oleic acid, a monounsaturated fatty acid that stimulates LD formation in cells, induced an increase of LD540 staining intensity in *Spg20+/+* MEFs. The LD540 intensity in oleic acid-treated *Spg20−/−* cells remained higher than in *Spg20+/+* cells, but not significantly different from *Spg20−/−* cells not treated with oleic acid (Fig. 5G). Together these results confirm a crucial role for spartin in LD maintenance. In particular, these data are consistent with the proposed role of spartin in the recruitment of AIP4 and AIP5 (18,19,24,27).

Spartin participates in cytokinesis

Since several recent studies have shown that spartin is involved in cytokinesis (21,38), we analyzed cell division in MEFs. *Spg20−/−* MEFs were larger than *Spg20+/+* cells (Supplementary Material, Fig. S7), and the number of multinucleated cells was far higher in *Spg20−/−* when compared with *Spg20+/+* MEFs (Fig. 6A and B), confirming that spartin participates in cell division. Analysis of the dynamics of cell movement showed that while velocities were similar, cultured *Spg20−/−* MEFs migrated further than *Spg20+/+* cells (Fig. 6C). Live imaging of cells also showed that cytokinesis was slowed in *Spg20−/−* cells when compared with *Spg20+/+* cells (Fig. 6D). Moreover, the number of division events was higher in *Spg20+/+* when compared with *Spg20−/−* cells over the same time period (compare Supplementary Material, Videos S5 [Spg20+/+] and S6 [Spg20−/−]). In addition, some *Spg20−/−* MEFs divided aberrantly, including instances where a single cell divided into three daughter cells (Supplementary Material, Video S7).

Spg20−/− mice exhibit an *in vivo* cytokinesis defect in chondrocytes

Since Troyer syndrome patients have short stature and other prominent skeletal anomalies that suggest dysfunctional bone development (13), we characterized the skeletal phenotype of *Spg20−/−* mice. Skeletons of postnatal day 1 (P1) and P28 *Spg20−/−* and *Spg20+/+* mice stained with Alcian blue/Alizarin red showed no gross histological abnormalities in epiphyseal growth plate structure during formation of the long bones of the appendicular skeleton (Fig. 6E and F and data not shown). Quantification of vertebral column length at P1 and P28 revealed no differences between *Spg20+/+* and *Spg20−/−* mice, and the sizes of tibia, femur, humerus and

ulna of *Spg20+/+* and *Sp20−/−* mice were similar at both P1 and P28 (data not shown). H&E-stained sections of knee joints of newborn *Spg20+/+* and *Spg20−/−* mice appeared grossly similar. However, multinucleated chondrocytes in *Spg20−/−* mice were significantly increased (Fig. 6G), suggesting that defective cell division in epiphyseal growth plates in the context of the much larger scale of human long bones could contribute to the short stature of patients with Troyer syndrome.

BMP signaling alterations in *Spg20−/−* cells

A number of HSP proteins, including spartin, act as inhibitors of the BMP signaling pathway (28). We analyzed the BMP signaling pathway in MEFs from *Spg20+/+* and *Spg20−/−* mice. Cells were serum starved for 20 h, then incubated with or without BMP4 for 1 h. After BMP4 stimulation, the pSmad/Smad ratio was significantly higher in *Spg20−/−* cells than in *Spg20+/+* cells (Fig. 7A and B), consistent with previously published spartin siRNA studies (28). Analysis of BMP receptor II (BMPRII) levels in cultured cerebral cortical neurons treated with or without BMP4 ligand for 1 h after a 4-h serum-starvation showed no significant differences in *Spg20−/−* neurons, under both BMP4-treated and untreated conditions (Fig. 7C). Though there was a trend toward an increase in pSmad phosphorylation in the *Spg20−/−* neurons, as seen in the MEFs (Fig. 7B), this did not reach statistical significance under these experimental conditions (Fig. 7C and D). Spartin protein levels in *Spg20+/+* MEFs and neurons were unchanged after BMP stimulation (Fig. 7A and E).

DISCUSSION

Troyer syndrome is a complicated HSP, with a number of clinical features in addition to the cardinal symptom of lower extremity spastic paraparesis, including short stature, bony defects, cognitive impairment, prominent spastic dysarthria and distal amyotrophy (10–14). Given this clinical presentation, it is not surprising that spartin has already been implicated in several cellular processes: endocytic trafficking and degradation of EGFR (17,39), regulation of the size and number of LDs (18,19,24), BMP signaling (28), ubiquitylation (17,19) and cytokinesis (21,38). However, it remains unclear how these cellular defects resulting from spartin loss underlie the neurodegeneration and other pathologies in Troyer syndrome patients. To analyze spartin function *in vivo*, we generated a *Spg20−/−* mouse model for Troyer syndrome. We observed clear effects on motor function in these mice and identified key cell biological abnormalities that provide compelling links to disease pathogenesis.

The increased axonal branching in cultured *Spg20−/−* cortical neurons is likely pathologically relevant, since altered branching has been observed in a number of other HSP model systems. In fact, a very similar increased branching phenotype is seen in a *Spg21* null mouse model for Mast syndrome (SPG21; ref. 36), a complicated HSP afflicting the Old Order Amish with considerable phenotypic similarity to Troyer syndrome (40). The widely expressed Mast syndrome
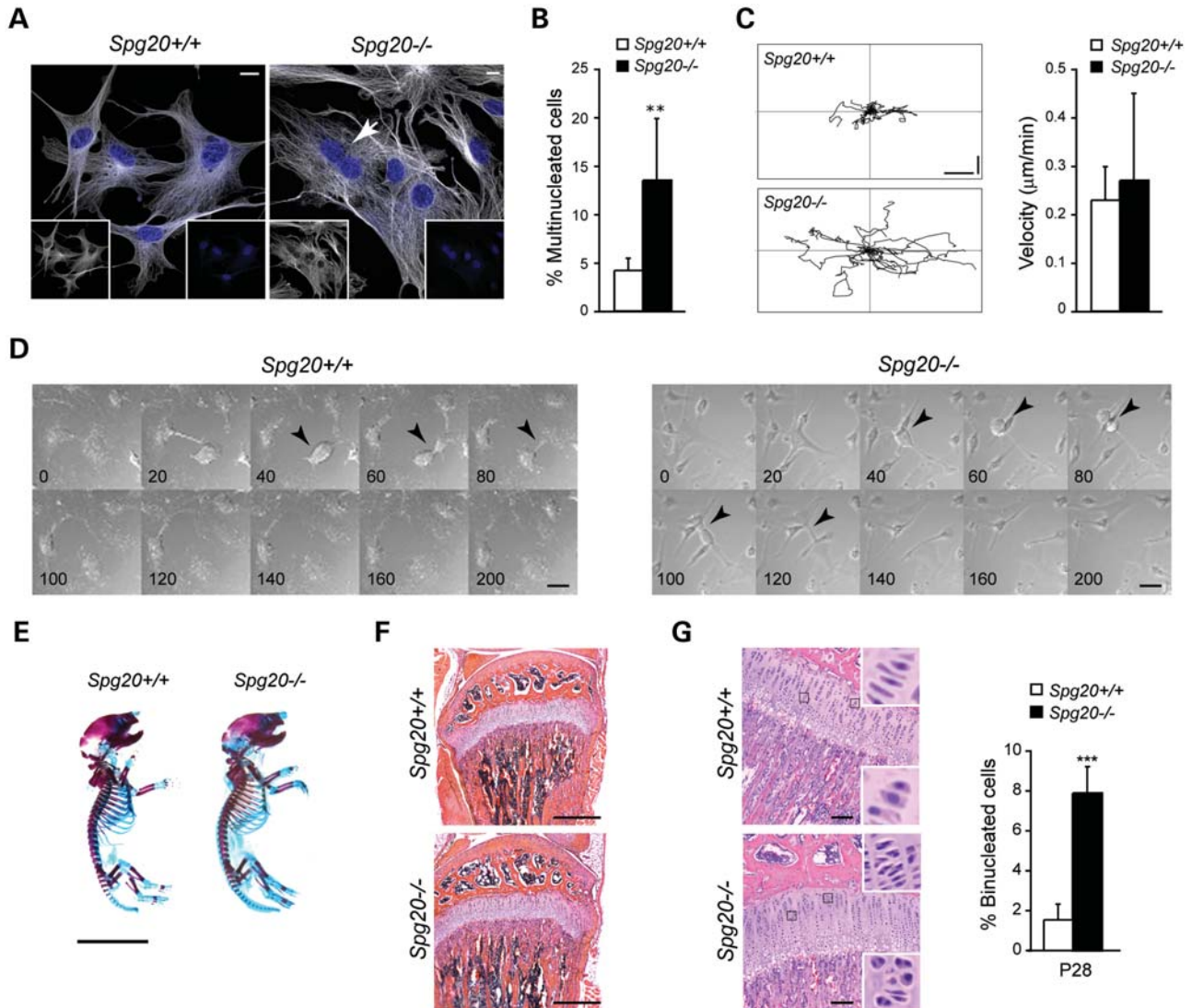
Figure 6. Cytokinesis defects in cells from *Spg20−/−* mice. (**A**) Representative MEFs from *Spg20+/+* and *Spg20−/−* mice stained with β-tubulin (white) and DAPI (blue). The merged image is shown, and an arrow identifies a binucleated cell. Individual channels are shown as insets. Scale bar, 10 μm. (**B**) Quantification of multinucleated MEFs in *Spg20+/+* and *Spg20−/−* mice. **$P < 0.01$. (**C**) Left, Representative trajectories of individual primary *Spg20+/+* and *Spg20−/−* MEFs from the frame-by-frame analysis of the time-lapse recordings during a 14-hour observation period. Vertical and horizontal scale bars, 50 μm. Right, Migration velocities of the indicated MEFs are graphed (means ± SD; $n = 20$). Migration data comprise at least 10 cells from 3 independent *Spg20+/+* and *Spg20−/−* pairs. (**D**) Time-lapse DIC images from 200 min of analysis, with times indicated. Arrowheads indicate dividing cells. Scale bar, 10 μm. (**E**) Whole mount Alcian Blue/Alizarin Red staining of *Spg20+/+* and *Spg20−/−* mouse skeletons at P1. Scale bar, 1 cm. (**F**) H&E-stained sections of the proliferative zone of the tibial epiphyseal growth plate of *Spg20+/+* and *Spg20−/−* mice. Scale bar, 500 μm. (**G**) Left, H&E-stained sections of the knee joint region of P28 *Spg20+/+* and *Spg20−/−* mice. The indicated areas are enlarged in the insets, demonstrating multiple binucleated chondrocytes. Right, Quantification of binucleated cells in growth plates of P28 *Spg20+/+* and *Spg20−/−* mice (means ± SD; $n = 3$ trials, with 100 cells per trial for each genotype). ***$P < 0.005$. Scale bar, 100 μm.

protein ACP33/maspardin functions as a negative regulator of CD4 signaling (41), and since neurons do not express CD4, it seems likely that ACP33/maspardin negatively regulates other growth factor/cytokine signaling pathways as well (36). A growth factor signaling pathway implicated in a number of different HSPs, including Troyer syndrome, is the BMP pathway. Indeed, Tsang *et al.* (28) described the effects of the knockdown of spartin as well as spastin (SPG4) and NIPA1 (SPG6) on the BMP signaling pathway, and in all cases these proteins acted as inhibitors of BMP signaling. Building on this theme, our analysis of BMP signaling in *Spg20−/−*

MEFs revealed that Smad1/5 phosphorylation was significantly increased when compared with wild-type *Spg20+/+* cells. Effects on cerebral cortical neurons in primary culture were less clear, but a similar trend toward increased Smad1/5 phosphorylation was observed in the *Spg20−/−* neurons.

In signaling pathways, there is often a close relationship between signal transduction and endocytic membrane traffic. For many plasma membrane receptors, cell surface receptor levels and endocytic processes, including ESCRT-mediated sorting, are important in regulating the signaling response (42,43). Previous work has already suggested that spartin is
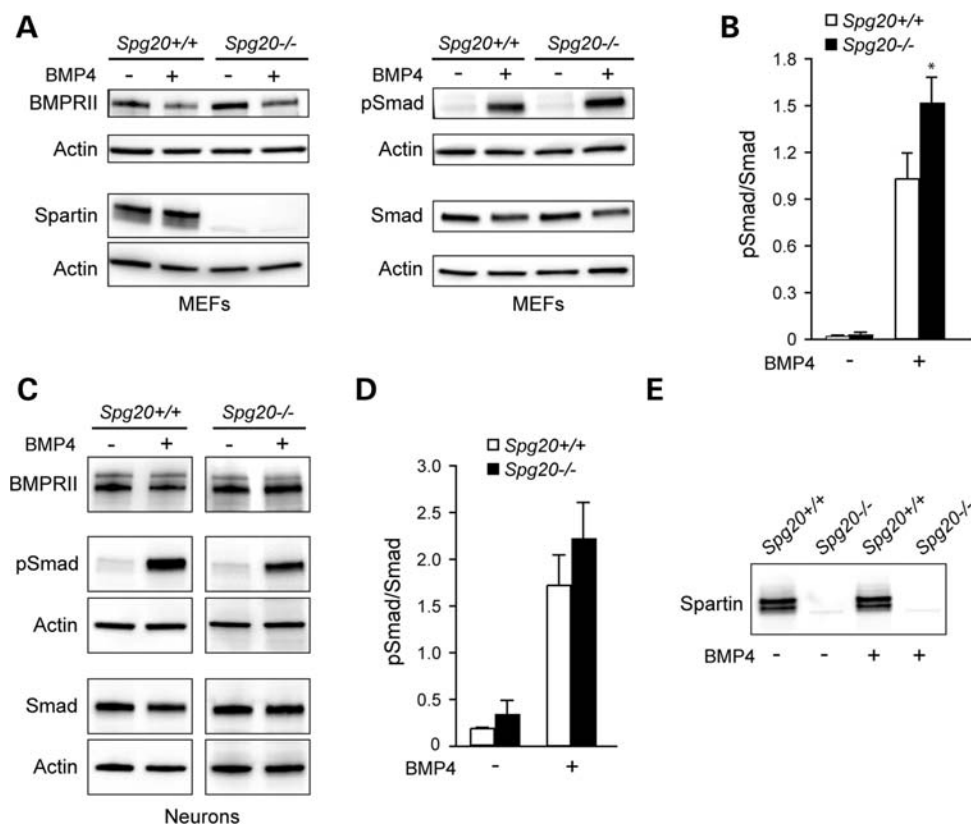
Figure 7. Alterations in BMP signaling and receptor degradation in *Spg20−/−* cells. (**A**) Immunoblot analysis of BMPRII, spartin, Smad and phospho-Smad (pSmad) expression levels in MEFs from *Spg20+/+* and *Spg20−/−* mice, with or without BMP4 addition as indicated. (**B**) Quantification of pSmad/Smad ratio in *Spg20+/+* and *Spg20−/−* MEFs (means ± SD; $n = 3$). $*P < 0.05$. (**C**) Immunoblot analysis of BMPRII, spartin, pSmad, Smad and EGFR protein levels in extracts from *Spg20+/+* and *Spg20−/−* cultured cerebral cortical neurons. (**D**) Quantification of pSmad/Smad ratio in *Spg20+/+* and *Spg20−/−* neurons (means ± SD; $n = 3$). (**E**) Immunoblot analysis of spartin levels in neurons from *Spg20+/+* and *Spg20−/−* mice, with or without BMP4 addition as indicated.

involved in endocytic trafficking of EGFR through interaction with Eps15 (17,39). Thus, we postulate that, in corticospinal neurons, spartin could be important for the trafficking of BMPRII, and thus regulate BMP signaling. Decreased degradation of other growth factor receptors that would similarly result in altered signaling could be impacted by a lack of spartin expression as well.

It remains uncertain whether the effects of spartin on BMP signaling are responsible for the changes in axon branching observed in *Spg20−/−* neurons. However, particularly compelling in this regard is the high selective interaction of spartin with the ESCRT-III protein IST1 (21). IST1 and another ESCRT-III protein, CHMP1B, interact with the SPG4 protein spastin, a microtubule-severing AAA ATPase with prominent effects on axon branching (21,34,37). Here, we found that overexpression of spartin in *Spg20−/−* primary neurons significantly decreased the number of axon branches, while expression of the structure-based spartin missense mutant F24D, unable to bind IST1 (21), did not suppress the spartin-dependent branching phenotype. Thus, interaction with IST1 is required for spartin-mediated effects on axon branching. Interestingly, the equivalent mutation in the spastin MIT domain, F124D, also blocks its interaction with IST1 (21,37). Overexpression of the ESCRT-III subunit IST1 and CHMP1B, both of which interact with spastin, in primary rat cortical neurons induces an increase in the number of axon branches (B.R., unpublished results). Taken together, these results are consistent with spartin functioning as an inhibitor of IST1 activity, possibly by preventing its interaction with spastin. In this scenario, IST1 might increase axon branching via the recruitment of spastin to branch points or by modulating its ATPase activity. The mechanisms underlying ESCRT-mediated effects on axon branching is clearly an important area for future investigation.

A particularly prominent and distinguishing feature of Troyer syndrome among other HSPs is the short stature of patients. We have previously observed that spartin knockdown by siRNA in HeLa cells results in defective cytokinesis, specifically the frequent failure to complete abscission (21), and here we demonstrate dramatic effects on chondrocyte division in the epiphyseal growth plates of developing bone. Although this did not lead to significant changes in the length of *Spg20−/−* mice, the massively increased scale of human bone length may be particularly impacted by this decreased cell proliferation, thus providing a compelling mechanism to explain the short stature of Troyer syndrome patients.

In our pathological analysis of several *Spg20−/−* and *Spg20+/+* mice, a large mesenchymal tumor was found compressing the cervical spinal cord in a single *Spg20−/−* mouse (Supplementary Material, Fig. S4). Although most parsimoniously ascribed to chance, this finding takes on increased significance because of a recent report that described

hypermethylation of *SPG20*, resulting in down regulation of spartin expression, as a novel biomarker for early detection of human colorectal cancer (38), in conjunction with an earlier study describing the involvement of spartin in cytokinesis (21). It seems reasonable to speculate that hypermethylation of the *SPG20* gene promoter is prominent not only in colon cancers and adenomas (38) but in other tumor types as well. The incidence of cancer in Troyer syndrome patients has not been reported, but will be an important area to emphasize in future investigation.

Dysfunction of the ESCRT complex can affect several cellular pathways in addition to cytokinesis. Recent data showed that functional ESCRT complexes are required for autophagic fusion and clearance (44), in particular during the normal degradation process of the EGFR (45). Very recently, spartin has been shown to bind to p62/sequestosome-1 (ZIP1 and ZIP3 in rats), a protein with key roles during autophagy that in turn interacts with protein kinase C (PKC)-ζ. Spartin is required for the localization of both p62/sequestosome-1 and PKC-ζ to LDs, and the presence of the overexpressed spartin/PKC-ζ/p62 complex increases LD size (46). These data are in excellent agreement with our observation that adipocytes are smaller in the adipose tissue of *Spg20−/−* female mice. Furthermore, a direct link of spartin to LD formation has been demonstrated in several studies, and spartin interacts with TIP47 and AIP4/AIP5 on LDs (18,19,24). Importantly, defects in lipid metabolism have been reported for a number of other HSPs (2,9). For instance, although autosomal recessive mutations in the *BSCL2* gene encoding the Berardinelli-Seip congenital lipodystrophy 2 protein (also known as seipin) cause congenital lipodystrophy, autosomal dominant mutations cause Silver syndrome (SPG17), an HSP with associated distal amyotrophy (47,48). Seipin localizes to the base of LDs, where it regulates adipocyte differentiation and LD formation (49). Also, SPG39 results from mutations in the gene encoding neuropathy target esterase (NTE), a serine esterase with phospholipase and lysophospholipase activities that localizes to the endoplasmic reticulum and LDs (50,51). NTE is a crucial factor in nervous system development and maintenance, and brain-specific knockout of NTE in mice leads to progressive neurodegeneration (52–55).

In summary, our analysis of the *Spg20−/−* mouse model for Troyer syndrome reveals multimodal functions for spartin as a probable adaptor protein in the regulation of cytokinesis, LD maintenance, and BMP signaling, with one or more of these functions likely mediating alterations in axon development and branching. Importantly, other HSP proteins function in each of these cellular themes. Thus, Troyer syndrome is a rare form of HSP that links pathogenically to other forms. The involvement of spartin as an adapter protein linking autophagy and ESCRT proteins has important implications for more general mechanisms of neurodegeneration.

MATERIALS AND METHODS

Generation and breeding of *Spg20* knockout mice

All animal experiments were conducted under research protocols approved by the NINDS/NIDCD Animal Care and Use Committee and/or the IACUC at Loyola University Chicago.

Spg20−/− mice were generated commercially (Xenogen Biosciences) on a C57BL/6J genetic background. For construction of the targeting vector, the mouse chromosome 3 sequence (nt # 55 170 000−55 250 000) was retrieved from the Ensembl database (http://www.ensembl.org) and used as a reference. BAC clone RP23-304A2 was used for generating homologous arms and Southern probes by PCR or the RED cloning/gap-repair method. The 5′ (2.5 kb) and 3′ (7.3 kb) homologous arms were generated by RED cloning/gap repair. They were cloned into CDLloxNw and pCR2.1 vectors, with fidelity confirmed by restriction digestion and end sequencing. The final vector was obtained by standard molecular cloning methods. Aside from homologous arms, the final vector also contained a LoxP-flanked Neo^r expression cassette [for positive selection of embryonic stem (ES) cells] and a diphtheria toxin subunit A (DTA) expression cassette (for negative selection of ES cells). Final vector construction was confirmed by restriction digestion and end sequencing analysis. *Not*I digestion was used to linearize the final vector for electroporation. External 5′ and 3′ probes were generated by PCR using proofreading TaKaRa LA Taq (Takara Bio) and tested using genomic Southern blot analysis for ES screening. They were cloned into the pCR2b.1-TOPO backbone, with confirmation by DNA sequencing. For genotyping, genomic DNA was isolated from tail snips using standard procedures. Gene-specific PCR was carried out with Taq DNA polymerase (Invitrogen) and primers specific for *Spg20* (forward: 5′-GTTAATCTGAGCCAGATTGTGCCCTG-3′), Neo^r cassette (forward: 5′-GGAAGATGGAACCGCT GGAGAGC-3′), and genomic reverse (5′-GGACAGAAT CCTGATTTATGCTTACAG-3′). The Neo^r cassette was subsequently removed by breeding *Spg20−/−* mice with Cre-expressing C57BL/6J mice. For subsequent breeding, one male and one female from sexual maturity (∼40 days) to 12 months of age were housed in the same cage. After gestation and delivery, P1 pups were sacrificed to generate neuronal cell cultures or else the young mice were weaned from their mother 21−28 days after birth.

Behavioral testing

Spg20+/+ and *Spg20−/−* mice at 4–7 months of age were compared in two different trials, with observers blinded to their genotype. To assess motor ability, mice were tested using a Med Associates ENV-575M 5 Station Rotarod Treadmill. Briefly, mice were placed on an elevated rod (3.2 cm in diameter) and monitored in three independent trials separated by at least 15 min for recovery. The speed was set to increase from 4 to 40 rpm, and animals were on the Rotarod for a maximum of 300 s. For video analysis using the Rotarod apparatus, 4-month-old mice were placed on an elevated rod and the speed was set to increase from 4 to 40 rpm, for a maximum of 300 s, as mentioned earlier. Videos were edited using Windows VideoMaker.

Grip strength was monitored quantitatively using a grip strength meter (Bioseb) with the same mice. The mice were allowed to hold a metal grid with their back paws (2-leg test) and gently and steadily pulled backwards horizontally by the tail following the axle of the sensor, until they could no longer hold the grid. Recorded value corresponds to the

maximum force developed by hind limbs of the animal (in grams).

Anatomical and histological analysis

Mice were transcardially perfused with 4% paraformaldehyde, and brain, spinal cord and skeletal muscle (gastrocnemius) were isolated and post-fixed in 5% paraformaldehyde for 16 h. Sections (50 μm thick) were cut with a cryostat (Leica CM3050S) and subsequently stained with H&E, Nissl, luxol fast blue, or Cresyl violet, or else immunostained as described previously (36).

Skeletal staining with Alcian blue/Alizarin red, histochemistry and immunostaining were carried out as described (56). Briefly, skeletal whole mounts of P1 or P28 mice were performed on eviscerated animals with the skin completely removed. Carcasses were fixed in 95% ethanol, transferred to acetone, and finally stained in 0.01% Alizarin Red S and 0.02% Alcian Blue 8GX (Sigma-Aldrich) in 5% acetic acid and 75% ethanol at 37°C. Samples were washed with water, cleared in 1% KOH (2–4 days for P1 mice, and 7–14 days for P28, with daily solution changes) and stored long-term in 50% glycerol (w/v) in phosphate-buffered saline (PBS). This procedure stains cartilage blue and calcium-containing tissues such as bone red.

Body adipose tissue composition was measured in non-anesthetized mice using an EchoMRI 3-in-1 Body Composition Analyzer (Echo Medical Systems). For histological analysis of adipose tissue, abdominal white adipose tissue was dissected from mice and frozen at −80°C. Thick sections (50 μm) were cut using a cryostat at −50°C, fixed with 4% formaldehyde, and stained with H&E. Imaging of sections was performed using a Zeiss LSM710 laser scanning confocal microscope (Carl Zeiss Microimaging), with data analysis using ImageJ software (NIH).

Antibodies

Mouse monoclonal antibodies were used against β-tubulin (IgG1, clone D66, Sigma-Aldrich), neuronal β-tubulin (14944302; Covance), actin (clone AC-40; Sigma-Aldrich), PLCγ-1 (2822; Cell Signaling) and Tau-1 (MAB3420; Chemicon). Rabbit polyclonal antibodies were used HA-epitope (ab9110; Abcam), spartin (13791; ProteinTech), IST1 (KIAA0174; GeneTex), synaptotagmin (gift from Dr Peter Low, Karolinska Institutet), PSD-95 (51–6900; Zymed Laboratories, Invitrogen), perilipin (34705; Cell Signaling), MAP2 (sc-20172; Santa Cruz Biotechnology), BMPRII (612292; BD Bioscience), EGFR (sc-03; Santa Cruz Biotechnology), Smad (97435; Cell Signaling) and phospho-Smad1/5 (95165; Cell Signaling). A chicken polyclonal antibody (IgY) against neurofilament protein NF-H was purchased from Covance (PCK-592P).

Tissue preparation and immunoblotting

Preparation of cell extracts, gel electrophoresis and immunoblotting were performed as described previously (33,57,58). Protein concentrations were determined using the Pierce BCA Protein Assay Reagent (Thermo Fisher Scientific) with bovine serum albumin as the standard. For immunoblotting, proteins were resolved by sodium dodecyl sulphate–polyacrylamide gel electrophoresis (SDS–PAGE) and then electrophoretically transferred to nitrocellulose. After blocking with non-fat milk/0.1% Tween 20/Tris-buffered saline (pH 7.5), antibodies (1–5 μg/ml) were added overnight at 4°C.

For whole tissue studies, mice were dissected, taking care that all white adipose deposits were removed, and tissues were weighed. After rinsing once with cold PBS, cold lysis buffer [150 mM NaCl; 50 mM Tris–HCl, pH 7.4; 1 mM ethylenediaminetetraacetic acid (EDTA); 1% NP-40; 0.5% deoxycholate; 0.1% SDS; Roche Complete Protease Inhibitor; 1 mM phenylmethylsulfonyl fluoride (PMSF) was immediately added at a ratio of 1:5–1:10 tissue to buffer (w/v). Samples were then homogenized using a Polytron homogenizer, sonicated briefly and centrifuged (4°C, 16 000 g, 30 min). The supernatants (20–30 μg protein) were subjected to SDS–PAGE and immunoblotted with the appropriate antibodies.

Most tissues were prepared as described previously (57). For preparation of adipose tissue, mice were dissected at 4 months and tissue was weighed. After rinsing once with cold PBS, the tissue was transferred immediately to cold lysis buffer [150 mM NaCl; 50 mM Tris–HCl, pH 7.4; 1 mM EDTA; 1% NP-40; 0.5% DOC; 0.8% SDS; Complete Protease Inhibitor (Roche); 1 mM PMSF] at a 1:5–1:10 tissue-to-buffer ratio (w/v). Signal quantifications were carried out with Image Lab Software (Bio-Rad) and normalized using an actin loading control signal.

Confocal immunofluorescence microscopy

A muscle staining protocol was adapted from Burgess *et al.* (59). Briefly, tibialis anterior muscles were isolated from adult mice and fixed in 5% paraformaldehyde in PBS for 4 h on ice. Samples were transferred to a blocking and permeabilizing solution of 5% normal goat serum and 0.5% Triton X-100 in PBS for 1 h before they were pressed between two glass slides for 15 min, then returned to blocking and permeabilizing solution. Samples were incubated overnight at 4°C with primary antibodies against NF-H, synaptotagmin, or PSD-95. After three 1-h washes in PBS containing 0.5% Triton X-100, samples were transferred to blocking/permeabilizing solution with Alexa Fluor 564 goat anti-mouse IgG$_1$ (Invitrogen) and α-bungarotoxin conjugated to Alexa Fluor 488 (B-13422; Invitrogen). After incubation overnight at 4°C, samples were washed three times for 1 h and mounted with Fluoromount-G.

For live-cell imaging experiments, MEFs were cultured on 2-well glass-bottom chambers (Lab-Tek II Chamber Slides; Nalge Nunc International). Time-lapse recordings were made using a Zeiss LSM710 confocal microscope (Zeiss/PeCon XL LSM 710S1 live-cell incubator system with TempModule S, CO$_2$ Module S1 and Heating Unit XL S) at 37°C in a 5% CO$_2$ humidified chamber. Images were obtained using a 40× 1.4 NA Plan-Apochromat oil differential interference contrast (DIC) objective as 1 μm z-stacks at 20 min intervals, together with a single DIC reference image. Images were exported in 8-bit TIFF format using NIH ImageJ software. For quantification studies, DIC images were used to determine

the timing of mitosis. Fluorescence images were processed with ImageJ and Adobe Photoshop 7.0 software.

To observe the midbody, cells plated on coverslips were fixed for 4 min with ice-cold methanol and blocked for 45 min with 10% goat serum, 0.1% Triton X-100 in PBS at room temperature. After three washes, coverslips were incubated with primary antibodies diluted in 1% goat serum. Alexa Fluor anti-rabbit and anti-mouse secondary antibodies (Invitrogen) were used at 1:300 dilution. Cells were counterstained with 4′,6-diamidino-2-phenylindole (DAPI; 0.1 mg/ml; Sigma-Aldrich) where indicated and mounted using Fluoromount-G. Cells were imaged using a Zeiss LSM710 confocal microscope with a 63×1.4 NA Plan-Apochromat oil DIC objective, and image acquisition was performed using LSM510 version 3.2 SP2 software (Carl Zeiss Microimaging). Images were processed with ImageJ, Adobe Photoshop, and Adobe Illustrator CS2 software.

Neuronal cultures and transfections

Primary cultures of mouse cerebral cortical neurons were prepared from P1 mice, plated at a density of $\sim 1.0 \times 10^4/\text{cm}^2$ on coverslips, and maintained and immunostained as described previously (36). Quantifications of cell length, cell breadth, cell area, form factor, bipolarity index and spreading index were performed according to Lepekhin *et al*. (60). For overexpression and biochemical studies, cells were transiently transfected with DNA plasmids using Amaxa nucleofector system (Lonza) for 3 day following the instructions of the manufacturer. The eukaryotic expression constructs for HA-spartin, HA-spartin F24D and HA-IST1 were described previously (17,21). Quantification of fluorecence intensity and measurements of axonal length and branching were carried out using ImageJ and NeuronJ (NIH) software, respectively.

Preparation of MEFs

Embryos derived from pregnant female *Spg20+/−* mice at day 14 post-coitum were used to generate *Spg20+/+* and *Spg20−/−* cells. Females were sacrified and the uterine horns were dissected out. Each embryo was separated from its placenta and the brain and dark red organs were excised. After washing with PBS, individual embryos were finely minced, suspended in trypsin–EDTA (Gibco), and incubated with gentle shaking at 37°C for 15 min. After adding 2 vol of fresh MEF medium [DMEM (high glucose; Gibco 41966-052), 10% fetal bovine serum, 1:100 (v/v) L-glutamine (200 mM; Gibco 25030-024) and 1:100 penicillin/streptomycin (Gibco 15140-122)] the remaining pieces of tissue were removed, and the supernatant was centrifuged for 5 min at 100 *g*. The cell pellet was resuspended in MEF medium, and the cells were plated.

BMP signaling and receptor degradation assays

MEFs were cultured to subconfluency and then serum starved for 20 h at 37°C. For neuronal studies, neurons were prepared from P1 mouse cerebral cortices as described previously (35) and plated at a density of $4–8 \times 10^6$ per 10 cm plate. For BMPRII and EGFR experiments, after 7 days *in vitro*

neurons were serum starved for 4 h, then either mock-treated or else treated with BMP4 ligand (20 µg/ml; Sigma B2680) for 1 h. The media were then removed, and cells were washed twice with PBS. Cells were scraped into extraction buffers: for MEFs (50 mM Tris–HCl pH 7.4; 150 mM NaCl; 1 mM EDTA; 0.1% SDS; 0.5% deoxycholate; 1 mM PMSF; Roche Complete Protease Inhibitor, EDTA-free; PhosSTOP), and for neurons (50 mM Tris–HCl pH 7.4; 150 mM NaCl; 1 mM EDTA; 1% SDS; 1 mM PMSF; Roche Complete Protease Inhibitor, EDTA-free; PhosSTOP). Samples were boiled for 7 min, and then centrifuged for 2 min at 16 000 *g* (Eppendorf 5415 D centrifuge). After protein quantification, SDS–PAGE sample buffer was added and samples were incubated at 65°C for 5 min and resolved by SDS–PAGE (20–25 µg total protein) immediately or stored at −80°C.

Oleic acid treatment and LD540 staining

To analyze LDs, MEFs cultured as decribed above were incubated with 100 mM oleic acid (Sigma-Aldrich) overnight. The next day, cells were fixed with 4% formaldehyde, permeabilized and immunostained with antibodies as described above. Then, cells were incubated with a solution of 0.1 µg/ml LD540 (61) (gift of Dr Christoph Thiele) in PBS for 5 min, washed and mounted in Fluoromount-G. Fluorescence images were acquired with a $63 \times$ objective as a series of the optical z-stacks spanning the entire cell, using the transmitted light of a Zeiss LSM710 laser scanning confocal microscope (Carl Zeiss Microimaging). The recording conditions were set to obtain a fluorescence signal below the saturation level. Cell boundaries were defined by applying a threshold to each of the z-sections. Total fluorescence was calculated using ImageJ. At least 10 cells were randomly selected and examined for each condition.

Statistical analysis

Results are expressed as the mean $\pm$ SD. Statistical analysis was performed using Student's *t*-test, assuming unequal variance, with $P < 0.05$ considered significant; Mann–Whitney U-statistics were used for skeletal comparisons. Asterisks indicate significant differences ($*P < 0.05$, $**P < 0.01$, $***P < 0.005$, $****P < 0.001$).

SUPPLEMENTARY MATERIAL

Supplementary Material is available at *HMG* online.

ACKNOWLEDGEMENTS

FUNDING

REFERENCES

1. Salinas, S., Proukakis, C., Crosby, A. and Warner, T.T. (2008) Hereditary spastic paraplegia: clinical features and pathogenetic mechanisms. *Lancet Neurol.*, **7**, 1127–1138.

2. Blackstone, C., O'Kane, C.J. and Reid, E. (2011) Hereditary spastic paraplegias: membrane traffic and the motor pathway. *Nat. Rev. Neurosci.*, **12**, 31–42.

3. Harding, A.E. (1983) Classification of the hereditary ataxias and paraplegias. *Lancet*, **1**, 1151–1155.

4. Fink, J.K. (2006) Hereditary spastic paraplegia. *Curr. Neurol. Neurosci. Rep.*, **6**, 65–76.

5. Soderblom, C. and Blackstone, C. (2006) Traffic accidents: molecular genetic insights into the pathogenesis of the hereditary spastic paraplegias. *Pharmacol. Ther.*, **109**, 42–56.

6. Dion, P.A., Daoud, H. and Rouleau, G.A. (2009) Genetics of motor neuron disorders: new insights into pathogenic mechanisms. *Nat. Rev. Genet.*, **10**, 769–782.

7. Park, S.H. and Blackstone, C. (2010) Further assembly required: construction and dynamics of the endoplasmic reticulum network. *EMBO Rep.*, **11**, 515–521.

8. Renvoisé, B. and Blackstone, C. (2010) Emerging themes of ER organization in the development and maintenance of axons. *Curr. Opin. Neurobiol.*, **20**, 531–537.

9. Blackstone, C. (2012) Cellular pathways of hereditary spastic paraplegia. *Annu. Rev. Neurosci.*, **35**, 25–47.

10. Cross, H.E. and McKusick, V.A. (1967) The Troyer syndrome: a recessive form of spastic paraplegia with distal muscle wasting. *Arch. Neurol.*, **16**, 473–485.

11. Patel, H., Cross, H., Proukakis, C., Hershberger, R., Bork, P., Ciccarelli, F.D., Patton, M.A., McKusick, V.A. and Crosby, A.H. (2002) *SPG20* is mutated in Troyer syndrome, an hereditary spastic paraplegia. *Nat. Genet.*, **31**, 347–348.

12. Proukakis, C., Cross, H., Patel, H., Patton, M.A., Valentine, A. and Crosby, A.H. (2004) Troyer syndrome revisited. A clinical and radiological study of a complicated hereditary spastic paraplegia. *J. Neurol.*, **251**, 1105–1110.

13. Bakowska, J.C., Wang, H., Xin, B., Sumner, C.J. and Blackstone, C. (2008) Lack of spartin protein in Troyer syndrome: a loss-of-function disease mechanism? *Arch. Neurol.*, **65**, 520–524.

14. Manzini, M.C., Rajab, A., Maynard, T.M., Mochida, G.H., Tan, W.-H., Nasir, R., Hill, R.S., Gleason, D., Al Saffar, M., Partlow, J.N. *et al.* (2010) Developmental and degenerative features in a complicated spastic paraplegia. *Ann. Neurol.*, **67**, 516–525.

15. Lu, J., Rashid, F. and Byrne, P.C. (2006) The hereditary spastic paraplegia protein spartin localises to mitochondria. *J. Neurochem.*, **98**, 1908–1919.

16. Robay, D., Patel, H., Simpson, M.A., Brown, N.A. and Crosby, A.H. (2006) Endogenous spartin, mutated in hereditary spastic paraplegia, has a complex subcellular localization suggesting diverse roles in neurons. *Exp. Cell Res.*, **312**, 2764–2777.

17. Bakowska, J.C., Jupille, H., Fatheddin, P., Puertollano, R. and Blackstone, C. (2007) Troyer syndrome protein spartin is mono-ubiquitinated and functions in EGF receptor trafficking. *Mol. Biol. Cell.*, **18**, 1683–1692.

18. Eastman, S.W., Yassaee, M. and Bieniasz, P.D. (2009) A role for ubiquitin ligases and Spartin/SPG20 in lipid droplet turnover. *J. Cell Biol.*, **184**, 881–894.

19. Edwards, T.L., Clowes, V.E., Tsang, H.T.H., Connell, J.W., Sanderson, C.M., Luzio, J.P. and Reid, E. (2009) Endogenous spartin (SPG20) is recruited to endosomes and lipid droplets and interacts with the ubiquitin E3 ligases AIP4 and AIP5. *Biochem. J.*, **423**, 31–39.

20. Milewska, M., McRedmond, J. and Byrne, P.C. (2009) Identification of novel spartin-interactors shows spartin is a multifunctional protein. *J. Neurochem.*, **111**, 1022–1030.

21. Renvoisé, B., Parker, R.L., Yang, D., Bakowska, J.C., Hurley, J.H. and Blackstone, C. (2010) SPG20 protein spartin is recruited to midbodies by ESCRT-III protein Ist1 and participates in cytokinesis. *Mol. Biol. Cell.*, **21**, 3293–3303.

22. Joshi, D.C. and Bakowska, J.C. (2011) SPG20 protein spartin associates with cardiolipin via its plant-related senescence domain and regulates mitochondrial Ca^{2+} homeostasis. *PLoS One*, **6**, e19290.

23. Ciccarelli, F.D., Proukakis, C., Patel, H., Cross, H., Azam, S., Patton, M.A., Bork, P. and Crosby, A.H. (2003) The identification of a conserved domain in both spartin and spastin, mutated in hereditary spastic paraplegia. *Genomics*, **81**, 437–441.

24. Hooper, C., Puttamadappa, S.S., Loring, Z., Shekhtman, A. and Bakowska, J.C. (2010) Spartin activates atrophin-1-interacting protein 4 (AIP4) E3 ubiquitin ligase and promotes ubiquitination of adipophilin on lipid droplets. *BMC Biol.*, **8**, 72.

25. Hurley, J.H. and Hanson, P.I. (2010) Membrane budding and scission by the ESCRT machinery: it's all in the neck. *Nat. Rev. Mol. Cell Biol.*, **11**, 556–566.

26. Rotin, D. and Kumar, S. (2009) Physiological functions of the HECT family of ubiquitin ligases. *Nat. Rev. Mol. Cell Biol.*, **10**, 398–409.

27. Alberts, P. and Rotin, D. (2010) Regulation of lipid droplet turnover by ubiquitin ligases. *BMC Biol.*, **8**, 94.

28. Tsang, H.T.H., Edwards, T.L., Wang, X., Connell, J.W., Davies, R.J., Durrington, H.J., O'Kane, C.J., Luzio, J.P. and Reid, E. (2009) The hereditary spastic paraplegia proteins NIPA1, spastin and spartin are inhibitors of mammalian BMP signalling. *Hum. Mol. Genet.*, **18**, 3805–3821.

29. Wang, X., Shaw, W.R., Tsang, H.T.H., Reid, E. and O'Kane, C.J. (2007) Drosophila spichthyin inhibits BMP signaling and regulates synaptic growth and axonal microtubules. *Nat. Neurosci.*, **10**, 177–185.

30. O'Connor-Giles, K.M., Ho, L.L. and Ganetsky, B. (2008) Nervous wreck interacts with thickveins and the endocytic machinery to attenuate retrograde BMP signaling during synaptic growth. *Neuron*, **58**, 507–518.

31. Bayat, V., Jaiswal, M. and Bellen, H.J. (2011) The BMP signaling pathway at the Drosophila neuromuscular junction and its links to neurodegenerative diseases. *Curr. Opin. Neurobiol.*, **21**, 182–188.

32. Charron, F. and Tessier-Lavigne, M. (2007) The Hedgehog, TGF-β/BMP, and Wnt families of morphogens in axon guidance. *Adv. Exp. Med. Biol.*, **621**, 116–133.

33. Zhu, P.-P., Soderblom, C., Tao-Cheng, J.-H., Stadler, J. and Blackstone, C. (2006) SPG3A protein atlastin-1 is enriched in growth cones and promotes axon elongation during neuronal development. *Hum. Mol. Genet.*, **15**, 1343–1353.

34. Solowska, J.M., Morfini, G., Falnikar, A., Himes, B.T., Brady, S.T., Huang, D. and Baas, P.W. (2008) Quantitative and functional analyses of spastin in the nervous system: implications for hereditary spastic paraplegia. *J. Neurosci.*, **28**, 2147–2157.

35. Raino, E., Martignoni, M., Cartelli, D., Crippa, F., Toldo, I., Siciliano, G., Di Bella, D., Taroni, F., Bassi, M.T., Cappelletti, G. and Rugarli, E. (2009) Pleitropic effects of spastin on neurite growth depending on expression levels. *J. Neurochem.*, **108**, 1277–1288.

36. Soderblom, C., Stadler, J., Jupille, H., Blackstone, C., Shupliakov, O. and Hanna, M.C. (2010) Targeted disruption of the Mast syndrome gene SPG21 in mice impairs hind limb function and alters axon branching in cultured cortical neurons. *Neurogenetics*, **11**, 369–378.

37. Yang, D., Rismanchi, N., Renvoisé, B., Lippincott-Schwartz, J., Blackstone, C. and Hurley, J.H. (2008) Structural basis for midbody targeting of spastin by the ESCRT-III protein CHMP1B. *Nat. Struct. Mol. Biol.*, **15**, 1278–1286.

38. Lind, G.E., Raiborg, C., Danielsen, S.A., Rognum, T.O., Thiis-Evensen, E., Hoff, G., Nesbakken, A., Stenmark, H. and Lothe, R.A. (2011) SPG20, a novel biomarker for early detection of colorectal cancer, encodes a regulator of cytokinesis. *Oncogene*, **30**, 3967–3978.

39. Bakowska, J.C., Jenkins, R., Pendleton, J. and Blackstone, C. (2005) The Troyer syndrome (SPG20) protein spartin interacts with Eps15. *Biochem. Biophys. Res. Commun.*, **334**, 1042–1048.

40. Simpson, M.A., Cross, H., Proukakis, C., Hershberger, R., Chatonnet, A., Patton, M.A. and Crosby, A.H. (2003) Maspardin is mutated in Mast syndrome, a complicated form of hereditary spastic paraplegia associated with dementia. *Am. J. Hum. Genet.*, **73**, 1147–1156.

41. Zeitlmann, L., Sirim, P., Kremmer, E. and Kolanus, W. (2001) Cloning of ACP33 as a novel intracellular ligand of CD4. *J. Biol. Chem.*, **276**, 9123–9132.

42. Polo, S. and Di Fiore, P.P. (2006) Endocytosis conducts the cell signaling orchestra. *Cell*, **124**, 897–900.
43. Wegner, C.S., Rodahl, L.M.W. and Stenmark, H. (2011) ESCRT proteins and cell signalling. *Traffic*, **12**, 1291–1297.
44. Rusten, T.E., Filimonenko, M., Rodahl, L.M., Stenmark, H. and Simonsen, A. (2008) ESCRTing autophagic clearance of aggregating proteins. *Autophagy*, **4**, 233–236.
45. Bache, K.G., Stuffers, S., Malerød, L., Slagsvold, T., Raiborg, C., Lechardeur, D., Wälchli, S., Lukacs, G.L., Brech, A. and Stenmark, H. (2006) The ESCRT-III subunit hVps24 is required for degradation but not silencing of the epidermal growth factor receptor. *Mol. Biol. Cell*, **17**, 2513–2523.
46. Urbanczyk, A. and Enz, R. (2011) Spartin recruits PKC-ζ via the PKC-ζ-interacting proteins ZIP1 and ZIP3 to lipid droplets. *J. Neurochem.*, **118**, 737–748.
47. Agarwal, A.K. and Garg, A. (2004) Seipin: a mysterious protein. *Trends Mol. Med.*, **10**, 440–444.
48. Ito, D. and Suzuki, N. (2009) Seipinopathy: a novel endoplasmic reticulum stress-associated disease. *Brain*, **132**, 8–15.
49. Fei, W., Du, X. and Yang, H. (2011) Seipin, adipogenesis and lipid droplets. *Trends Endocrinol. Metab.*, **22**, 204–210.
50. Rainier, S., Bui, M., Mark, E., Thomas, D., Tokarz, D., Ming, L., Delaney, C., Richardson, R.J., Albers, J.W., Matsunami, N. *et al.* (2008) Neuropathy target esterase gene mutations cause motor neuron disease. *Am. J. Hum. Genet.*, **82**, 780–785.
51. Kienesberger, P.C., Lass, A., Preiss-Landl, K., Wolinski, H., Kohlwein, S.D., Zimmermann, R. and Zechner, R. (2008) Identification of an insulin-regulated lysophospholipase with homology to neuropathy target esterase. *J. Biol. Chem.*, **283**, 5908–5917.
52. Vose, S.C., Fujioka, K., Gulevich, A.G., Lin, A.Y., Holland, N.T. and Casida, J.E. (2008) Cellular function of neuropathy target esterase in lysophosphatidylcholine action. *Toxicol. Appl. Pharmacol.*, **232**, 376–383.
53. Read, D.J., Li, Y., Chao, M.V., Cavanagh, J.B. and Glynn, P. (2009) Neuropathy target esterase is required for adult vertebrate axon maintenance. *J. Neurosci.*, **29**, 11594–11600.
54. Moser, M., Li, Y., Vaupel, K., Kretzschmar, D., Kluge, R., Glynn, P. and Buettner, R. (2004) Placental failure and impaired vasculogenesis result in embryonic lethality for neuropathy target esterase-deficient mice. *Mol. Cell. Biol.*, **24**, 1667–1679.
55. Akassoglou, K., Malester, B., Xu, J., Tessarollo, L., Rosenbluth, J. and Chao, M.V. (2004) Brain-specific deletion of neuropathy target esterase/ swisscheese results in neurodegeneration. *Proc. Natl. Acad. Sci. USA*, **101**, 5075–5080.
56. Aszódi, A., Chan, D., Hunziker, E., Bateman, J.F. and Fässler, R. (1998) Collagen II is essential for the removal of the notochord and the formation of intervertebral discs. *J. Cell Biol.*, **143**, 1399–1412.
57. Zhu, P.-P., Patterson, A., Lavoie, B., Stadler, J., Shoeb, M., Patel, R. and Blackstone, C. (2003) Cellular localization, oligomerization, and membrane association of the hereditary spastic paraplegia 3A (SPG3A) protein atlastin. *J. Biol. Chem.*, **278**, 49063–49071.
58. Park, S.H., Zhu, P.-P., Parker, R.L. and Blackstone, C. (2010) Hereditary spastic paraplegia proteins REEP1, spastin, and atlastin-1 coordinate microtubule interations with the tubular ER network. *J. Clin. Invest.*, **120**, 1097–1110.
59. Burgess, R.W., Peterson, K.A., Johnson, M.J., Roix, J.J., Welsh, I.C. and O'Brien, T.P. (2004) Evidence for a conserved function in synapse formation reveals *Phr1* as a candidate gene for respiratory failure in newborn mice. *Mol. Cell. Biol.*, **24**, 1096–1105.
60. Lepekhin, E.A., Walmod, P.S., Berezin, A., Berezin, V. and Bock, E. (2001) Evaluation of cell morphology. Methods Mol. Biol*.*, 161, 85–100.
61. Spandl, J., White, D.J., Peychl, J. and Thiele, C. (2009) Live cell multicolor imaging of lipid droplets with a new dye, LD540. *Traffic*, **10**, 1579–1584.